
Article:
Liu, X., Lai, Y. orcid.org/0000-0002-9987-0975, Fisk, C. et al. (3 more authors) (2024) Experimental investigation on the effects of a mesh in the downstream region of a combustion-driven Rijke tube on self-excited thermoacoustic oscillations. Experimental Thermal and Fluid Science, 150. 111061. ISSN: 0894-1777

https://doi.org/10.1016/j.expthermflusci.2023.111061

Experimental Thermal and Fluid Science 150 (2024) 111061

Contents lists available at ScienceDirect

Experimental Thermal and Fluid Science

journal homepage: www.elsevier.com/locate/etfs

Experimental investigation on the effects of a mesh in the downstream region of a combustion-driven Rijke tube on self-excited thermoacoustic oscillations

Xuanqi Liu [a,b], Yufeng Lai [c,*], Callum Fisk [c], Jon Willmott [c], Huaichun Zhou [a,b], Yang Zhang [d,*]

[a] School of Low-Carbon Energy and Power Engineering, China University of Mining and Technology, Xuzhou 221116, China
[b] Research Center for Smart Energy, China University of Mining and Technology, Xuzhou 221116, China
[c] Department of Electronic and Electrical Engineering, The University of Sheffield, Sheffield S1 3JD, United Kingdom
[d] Department of Mechanical Engineering, The University of Sheffield, Sheffield S1 3JD, United Kingdom

ARTICLE INFO

Keywords:
Thermoacoustics
Combustion instabilities
Nonlinear oscillation
Thermal imaging
Schlieren imaging

ABSTRACT

Self-excited thermoacoustic oscillations are undesirable in most combustion systems due to their negative influence on combustion efficiency and structural vibration. Nonlinear thermoacoustic oscillations driven by combustion can be sensitive to changes in the heat and flow conditions. Therefore, a comprehensive study on self-excited thermoacoustic oscillations was conducted to investigate the effect of incorporating a woven mesh with varying mesh numbers and positions into the downstream region of a Rijke tube. This study determined system frequency and amplitude response and revealed dynamic properties of the system by applying recurrence analysis. To obtain temperature distributions, a thermal imaging system was employed, comprising a short wavelength infrared (SWIR) camera for the mesh and a long wavelength infrared (LWIR) camera for the tube wall. A high-speed schlieren imaging system was utilised for visualising heat and flow conditions at the tube end. The study demonstrated the effect of including a mesh in changing the oscillation eigenfrequency, suppressing the oscillation amplitude by up to 50 % and influencing the system dynamics. Higher mesh number demonstrated greater effectiveness. The captured thermal and schlieren images clearly evidenced the mesh's significant influence on the downstream heat and flow conditions. The insights gained from this work provide a potential control method of self-excited, nonlinear thermoacoustic oscillations.

1. Introduction

Thermoacoustic instabilities triggered in a combustion system are usually caused by unstable combustion process, and constitute a major concern in various combustion systems. This is due to their negative influences on combustion efficiency and system integrity. It has been found that the thermoacoustic could be triggered in both fuel lean and rich conditions with different types of fuel [1–5]. Therefore, an enhanced understanding of thermoacoustic instabilities can be crucial for the development of more efficient and robust combustion systems.

Rayleigh criterion states that the self-sustained thermoacoustic oscillation is initiated by the coupling of heat and pressure fluctuations, and Rayleigh Index can quantify the degree of this coupling effect [6–8]. In a combustion system, unsteady heat release is predominantly caused by perturbations of the flame area and combustion-flow interactions, and it is understood to be the primary causes of acoustic radiation [9–11]. Thermoacoustic oscillations are generally nonlinear and can exhibit different characteristics such as limit-cycle oscillations, quasi-periodicity and chaotic oscillations [12–16]. These characteristics of self-excited nonlinear thermoacoustic oscillation can vary over time by presenting different system behaviours and changes in system states [12,14,17–21]. The analysis of the nonlinear system dynamics can be adequate for providing the understanding of the system behaviour and tracing its transitions. Recurrence analysis for indicating the changes in system state is a direct and efficient way to study the nonlinear dynamics of unstable combustion [5,17,21,22]. The dynamic properties of the system, such as system state variations and periodicity, can be intuitively indicated by identifying the structural properties in the recurrence plot (RP) [23]. Recurrence quantification analysis (RQA) can further quantify the system dynamics through statistical measures of the structural properties in the RP.

* Corresponding authors.
E-mail addresses: y.lai@sheffield.ac.uk (Y. Lai), yz100@sheffield.ac.uk (Y. Zhang).

https://doi.org/10.1016/j.expthermflusci.2023.111061
Received 9 August 2023; Received in revised form 19 September 2023; Accepted 20 September 2023
Available online 24 September 2023

Nomenclature

D	Embedding dimension
E_{RMS}^{upper}	Upper p(t) RMS envelope
f_{eigen}	Eigenfrequency
l	Length of diagonal line
$\dot{m}_{CH_4}$	Methane flowrate
N	Number of point for RP
N_{pixel}	Number of pixels
p(l)	Probability of appearance for the diagonal line with a length of l
P(l)	Histogram of diagonal line
p_{rms}	Root mean square amplitude
p(t)	Pressure time series
P_{rms}^{Mesh}; $P_{rms}^{No\ Mesh}$	p_{rms} of mesh/No mesh cases
R	Recurrence matrix
T_{mesh}^{mean}	Mean mesh temperature
T_{local}	Local temperature of each pixel
$\overline{T}_{mesh}$	Time-averaged temperature
$\mathbf{x}_t$	Space vector
ε	Threshold for RP
τ	Time delay
Φ	Equivalence ratio
Θ	Heaviside function

Combustion parameters and flame dynamics can also have impacts on self-sustained oscillations. It has been found that equivalence ratio and flow conditions can affect the eigenfrequency, oscillation mode and stability of the system [2,5,9,17,24–27]. It has also been found that the system could transit from the periodic to quasi-periodic mode under specific equivalence ratios and overall heat power [2,28]. For a Rijke tube system with a flame holder, some studies focused on the effect of the hydrodynamic region which surrounds the flame holder on the system response. The effect of flame position, mean upstream and downstream temperature, and tube diameter on the oscillation behaviour have been theoretically and experimentally verified through the hydrodynamic region theory. Besides, these parameters and flow conditions also play critical roles in other types of thermoacoustic systems without a flame holder [8,29,30].

Currently, the majority of control schemes for thermoacoustic instabilities are passive, due to their high reliability and cost efficiency [9]. Passive control methods are implemented by modifying the system parameters that can influence the heat release or acoustic properties. For example, it has been found that adding perforated plate structures upstream in the combustion chambers can effectively mitigate thermoacoustic instabilities by attenuating the acoustic wave [9,31–33]. The attenuation is attributed to the creation of vortices at the orifices edge on the perforated plate. These vortices provide acoustic impedance that dissipates the acoustic energy, thereby mitigating oscillations [34,35]. Rayleigh conductivity of a perforated plate can be positively related to the perforated hole diameter and the distance between each hole. Alterations in these variables are related to the attenuation effect on both the oscillation amplitude and frequency response [36]. It has also been reported that the acoustic damping effect of a plate with compact holes would be more substantial when mitigating high-pressure oscillations [32]. Perforated structures in the downstream region can also influence the system, such as a perforated liner placed at the downstream region of the system can effectively control and suppress thermoacoustic oscillation [37–40]. The bias flow can significantly increase the absorption coefficient of perforated liner and acoustic impedance which further leads to a greater suppression effect [38,40].

Therefore, in a combustion system, the structures located downstream of the flame or combustion chamber can play a critical role in impacting the performance of system. Because the downstream flow and heat conditions can affect the characteristics of the potentially initiated thermoacoustic instabilities and the system behaviour [4,38]. Perforated-like structures, such as diffusers and nozzle guide vanes located downstream of combustion chambers and prior to the turbine, are commonly present in most existing gas turbine engines. They can play vital roles in regulating the flow of hot gases in this region and potentially influence the initiation of thermoacoustic oscillations, ultimately affecting the performance of combustion systems.

Some studies have investigated the effects of perforated structures on attenuating thermoacoustic oscillation in the combustion system; however, the effects of placing a perforated plate in the downstream region of the chamber on the eigenfrequency, oscillation amplitude and system properties are not yet fully understood. Meanwhile, the woven mesh, as another type of common perforated structure to provide flow conditioning, has not been extensively employed to control thermoacoustic instabilities. And its effect on acoustic attenuation is less understood in combustion systems. It has been found that including a woven mesh can result in acoustic pressure losses [41]. Therefore, this study aims to investigate the effect of woven mesh on suppressing and characterising the thermoacoustic oscillation in a Rijke tube. The effects of woven meshes with different mesh numbers and positions were investigated. A synchronised system consisting of a short wavelength infrared (SWIR) camera and pressure field microphones was utilised to obtain synchronised mesh temperature and pressure fluctuation data. A long wavelength infrared (LWIR) camera was used to obtain the temperature distribution of the tube surface, whilst a high-speed schlieren imaging system was utilised to investigate the heat and flow conditions above the mesh.

2. Experimental and data processing method

2.1. Experimental setup

In this study, a vertically placed, open-ended Rijke tube was utilised to trigger the thermoacoustic oscillation. The experimental setup used in this study is shown in Fig. 1. The tube was made of quartz with a length of 1 m and an inner diameter of 40 mm. The self-sustained thermoacoustic oscillation in this study was driven by a premixed methane-air flame with different equivalence ratios (Φ) ranging from 1.4 to 2.2 in increments of 0.2. The burner with a honeycomb flame holder was placed in the lower quarter of the tube (L/4). The height of the burner was measured from the bottom end of the tube to the top of the flame holder. A honeycomb flame holder with a blockage ratio of 22% was fixed at the top of the nozzle. It has been found that the critical blockage ratio that can affect the thermoacoustic oscillation is 25% [42], which means the honeycomb flame holder applied in this study has negligible effect on the oscillation. A piezo spark igniter was utilised to ignite the flame by generating a single spark. Once the flame was ignited, a stabilisation time of 3 min was allowed to ensure the oscillation is fully developed. The different Φ were obtained by changing the air flow rate while keeping the methane flow rate ($\dot{m}_{CH_4}$) the same. Both air and methane gases were controlled by corresponding Aalborg GFC17 flow controllers. The have accuracies of 0.05% for methane and 0.1% for air. The $\dot{m}_{CH_4}$ in this study was 0.8 L/min and the corresponding air flow rate was determined based on the required Φ. The experiments were also conducted with an $\dot{m}_{CH_4}$ of 0.65 L/min and 0.95 L/min to confirm the findings that were obtained from the present work.

Three different stainless steel (304L) woven meshes with mesh numbers of 10, 20 and 30 (Mesh 10, Mesh 20 and Mesh 30, respectively)

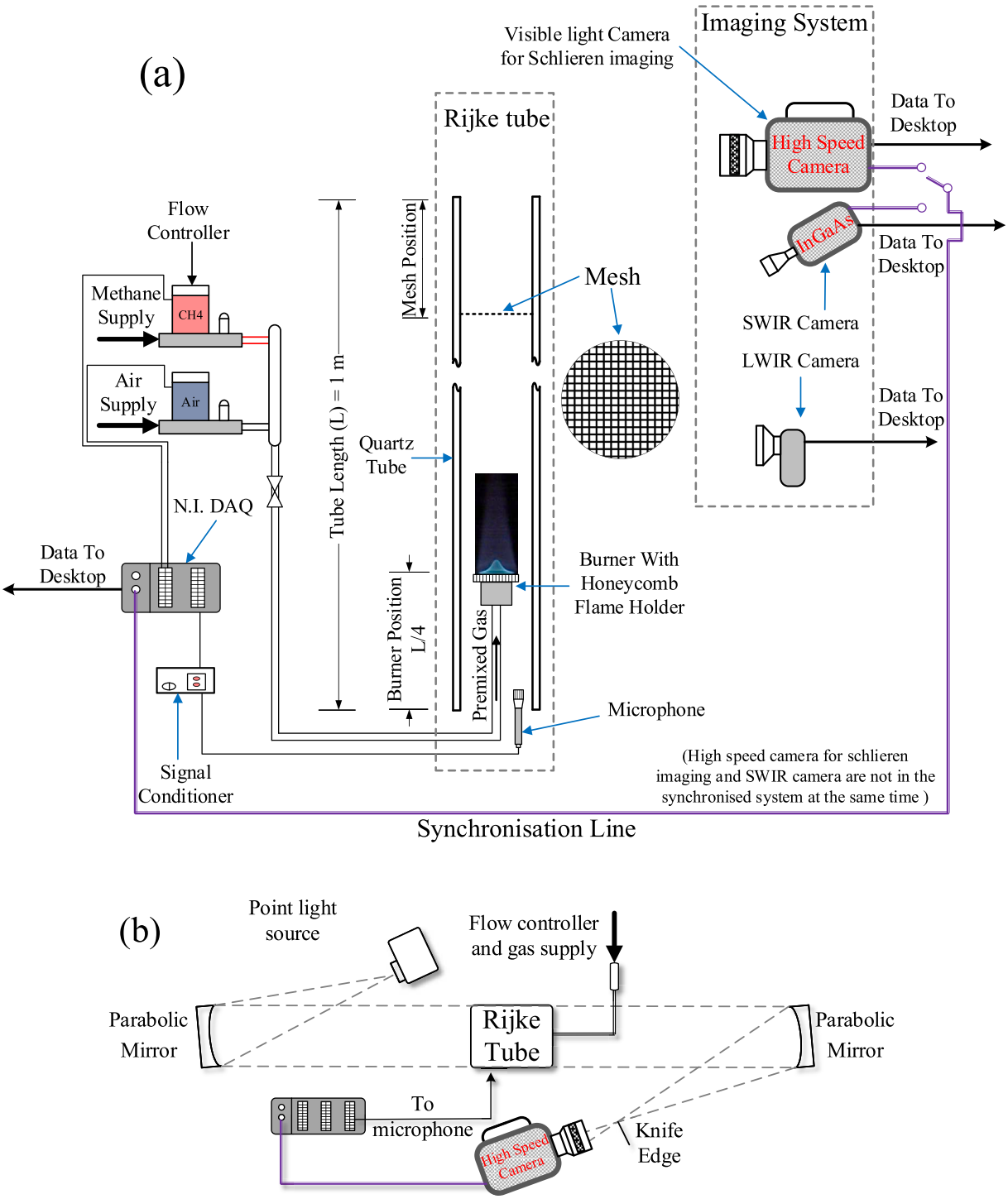

Fig. 1. Schematic figure of the experiment setup and data acquisition system: (a) the general setup, () Schlieren imaging system.

were investigated in this study. The specifications of the meshes utilised in this study are shown in Table 1. The mesh position was measured from the top of the tube to the position of the mesh. The mesh was placed at the top end of the tube and at distances of L/4, L/6, L/8, and L/12 to determine the influence of mesh position on the system behaviours.

Table 1
Specifications of the meshes utilised in this study.

Mesh Number	10	20	30
Nominal Aperture (mm)	1.98	0.915	0.567
Wire Diameter (mm)	0.56	0.355	0.28
Open Area	61%	52%	45%

A pressure-field microphone unit (model PCB 377C10 with a pre-amplifier PCB 426B03) was utilised to measure the pressure fluctuation time series at a sampling rate of 100,000 Hz. The unit was placed at the lower end of the tube to ensure that the ambient temperature does not exceed its maximum operating temperature, and the diaphragm of the microphone is perpendicular to the direction of pressure oscillation. Before every experiment, the microphone was calibrated against a 10 Pa signal at a frequency of 1000 Hz. The microphone was connected to an NI-9205 Voltage Input Module, which was connected to the Chassis

cDAQ-9178.

The thermal imaging system consisted of a Hamamatsu C12741-03 InGaAs SWIR camera, and a PyrOptik LWIR camera (model LW160). The SWIR camera was implemented to obtain the temperature of the mesh at a frame rate of 60 frames per second (FPS), whilst the LWIR camera obtained the tube wall temperature distribution. A Photron FASTCAM SA-4 high speed camera was utilised in the schlieren imaging system to capture the schlieren image for investigating the heat and flow conditions at the top tube end under the self-excited thermoacoustic oscillation. The SWIR camera was synchronised with the microphone and the thermocouples through the synchronising port on the Chassis cDAQ-9178. The schlieren imaging system was also synchronised with the microphone unit in the same way.

2.2. IR camera calibration and image processing

The InGaAs SWIR camera captures 60 frames per second (fps) at a resolution of 2048 × 2048 pixels, which is ideal for monitoring the fluctuation of the mesh temperature temporally. A bandpass filter was utilised to restrict the spectral sensitivity in the range of 1490 nm – 1500 nm, for obtaining an accurate temperature reading from 300 °C to 700 °C. A 100 mm prime lens with macro focusing was mounted with the camera, the optical aperture was fixed at f/4. The radiance calibration was based on Planck's Law using the method described by Lai et al. [43,44]. 100 images of a blackbody reference source were captured and averaged (emissivity ~ 0.99) between 300 °C and 700 °C, in increments of 50 °C. The zero offset of the camera was determined by averaging 100 images with the lens covered. The calibrated radiance temperature is shown in Fig. 2 (a) with the residuals. After calibration, the measured uncertainty was less than 1%. The mesh was made of polished stainless steel, type 304, which has a reported emissivity in the range of 0.2–0.35 [45]. Considering the high-temperature and air entrainment conditions inside the tube, we determined the emissivity of the mesh to be a fixed value of 0.3. The transmission of the tube was measured at different temperatures, which was 92.91% on average. The transmission loss has been calculated as a correction of the measured temperature.

The LWIR camera is sensitive to 8 μm – 14 μm, allowing accurate temperature measurements from ambient to 400 °C. The camera has a 640 × 512 pixels resolution, and the frame rate was fixed at 9 Hz. 100 images were captured and averaged to obtain the camera signal (DL) using a blackbody furnace (emissivity ~ 0.99) in the range of 50 °C to 400 °C. Fig. 2 (b) shows the calibration curve and measured uncertainty (red line). The fitted curve shows a good agreement with the blackbody temperature (R^2 = 0.9989). The maximum residual was found to be under 5 °C within this temperature range, which provided adequate performance for tube surface temperature monitoring. The tube was made of quartz glass, which has a reported emissivity of 0.93 [46]. The digital level captured by the LWIR camera was corrected based on the emissivity before any calculation.

The raw image of the mesh was then processed to obtain the temperature of the mesh and eliminate the background signal at the position of the mesh holes. A series of imaging processing methods, including thresholding, rescaling for contrast enhancement, and binarisation based on the adaptive threshold were applied to extract the portions of mesh wires in the region of interest (ROI). An example is shown in Fig. 3.

The mean mesh temperature (T_{mesh}^{mean}) was obtained from the ratio of the local temperature to the area of the mesh wire in order to eliminate the nonuniformity of the temperature distribution, shown in Eq. (1),

$$T_{mesh}^{mean} = \frac{\sum T_{local}}{N_{pixel}} \tag{1}$$

where T_{local} denotes the local temperature of the mesh for each pixel, which is considered as the mesh wire, as shown in Fig. 3(c). N_{pixel} is the total number of the corresponding pixels.

2.3. Recurrence analysis

The change and recursiveness of system states can be a crucial characteristic for describing the behaviour of a complex dynamical system since the system state can be varied with time. A recurrence plot (RP) can indicate the state changes and dynamic properties from the phase space via the structural properties of the plot, which is applicable for the investigation of self-excited and external-forced thermoacoustic instabilities [17,22,47,48]. In this study, the space vector of the trajectory in the phase space was obtained by using Takens' theorem [49]. The discrete time series of pressure fluctuations ($p(t)$), can be expressed using Eq. (2),

$$\mathbf{x}_t(D) = (p(t), p(t-\tau), p(t-2\tau), \cdots, p(t-(D-1)\tau)) \tag{2}$$

where $\mathbf{x}_t(D)$ is the space vector at time t with an embedding dimension of D, and τ is the time-delay. An appropriate value for τ is critical for constructing the phase space and the trajectory in the phase space. It is suggested that the proper value of τ can be estimated by either autocorrelation functions or the average mutual information method [1,17]. An inappropriate value of τ can result in an incorrect trajectory with incorrect correlation and attractors [1], leading to failure in indicating the system characteristics. In this study, τ was determined based on the first zero-crossing point from the autocorrelation functions since the system generally presented relatively high periodicity and low complexity. Based on the $\mathbf{x}_t(D)$, the lag-constructed RP can be generated by obtaining the recurrence matrix, **R**. **R** is a binary matrix which is defined using Eq. (3),

$$\mathbf{R}_{i,j} = \Theta\left(\varepsilon - \|\mathbf{x}_i - \mathbf{x}_j\|\right) \; i, j = 1, 2, 3, \cdots, N \tag{3}$$

where $\mathbf{x}_i$ and $\mathbf{x}_j$ are the $\mathbf{x}_t(D)$ at t = i, j, respectively. $\|\mathbf{x}_i - \mathbf{x}_j\|$ is the norm of the difference between $\mathbf{x}_i$ and $\mathbf{x}_j$. Θ is the Heaviside function. ε is the predefined threshold to determine whether two points on the

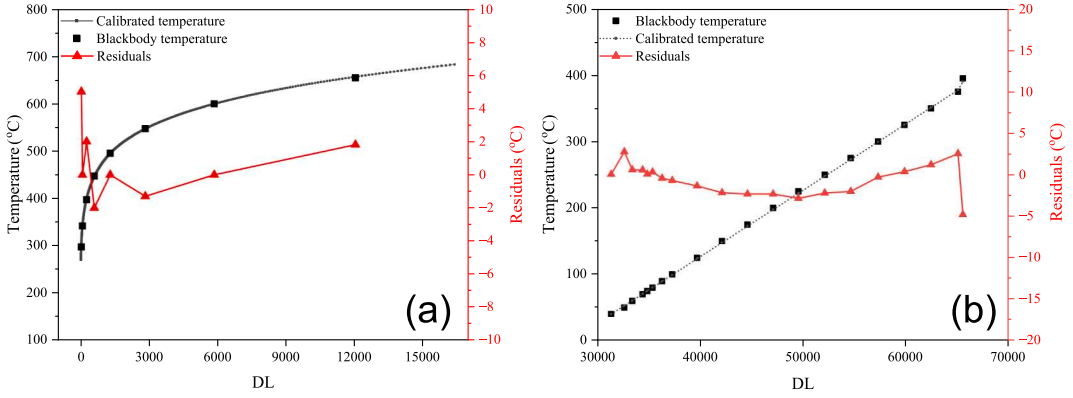

Fig. 2. Radiance calibration curve and uncertainty of measured temperature. (a): InGaAs SWIR camera and (b): LWIR camera.

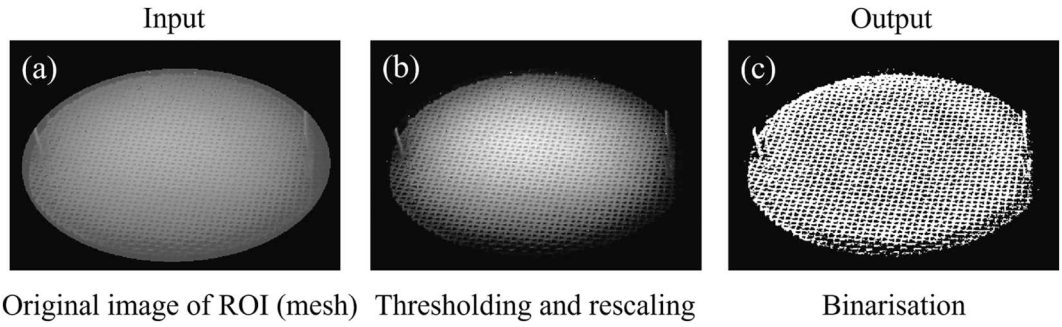

Fig. 3. An example of imaging processing for extracting the portions of mesh wires, (a) Crop the ROI from the original image, (b) Threshold the temperature (above 300 °C) and contrast adjustment (rescaling), (c) Binarisation.

trajectory can be considered recurrent. Choosing an appropriate value of ε is critical for the recurrence analysis, as the improper selection of ε can result in significant error [23,50]. In this study, the threshold is set to 15% of the standard deviation of the pressure fluctuations time series [51]. An inappropriate high sampling rate would result in a great determinism (DET) value which could lead to difficulties in implying the difference in the characteristics of highly periodic systems [52]. Therefore, a down-sampling process was performed to meet the suggested data points per period of 8 to 10 points [22]. The embedding dimension for the recurrence analysis can also be critical since improper D can result in spurious correlations and orthogonal structures to the line of identity (LOI, $\mathbf{R}_{i,i} = 1$). In this study, D was set as 3 for all cases according to the results of the false nearest neighbours (FNN) method [17,23].

To quantify the system dynamics through the structural properties in the RP, recurrence quantification analysis (RQA) was conducted to obtain the statistical measurements of the RP. The statistical measures of diagonal structures can efficiently indicate the stability of the system state and its complexity. In this study, the measures based on the diagonal structures, including determinism (DET), Shannon Entropy (ENT), and the average diagonal line length (ADL), were applied to investigate the effects of the mesh on the system dynamics. DET is defined as the ratio of the recurrence points which forms the diagonal line to all the recurrence points. It can indicate the occurrence probability of similar system states for the system. The ADL provides the degree of parallelism for the system since it can show the diverging rate of the two segments in the trajectory. For the complexity of the RP in respect of diagonal structures, ENT enables the quantitative measurement of system complexity. DET, ADL and ENT can be calculated using Eq. (4), Eq. (5) and Eq. (6), respectively,

$$\mathrm{DET} = \frac{\sum_{l=l_{min}}^{N} lP(l)}{\sum_{l=1}^{N} lP(l)} \tag{4}$$

$$\mathrm{ADL} = \frac{\sum_{l=l_{min}}^{N} lP(l)}{\sum_{l=min}^{N} P(l)} \tag{5}$$

$$\mathrm{ENT} = -\sum_{l=l_{min}}^{N} p(l)\ln p(l) \tag{6}$$

where N represents the number of points for recurrence analysis. l denotes the length of the diagonal line. l_{min} is the minimum diagonal line length, which was set to 2 in this study. P(l) is the histogram of the diagonal line with the length l. Based on P(l), the probability of appearance for the diagonal line with a length of l, p(l), can be defined as $p(l) = P(l)/N_l$, where N_l is the number of diagonal lines.

3. Result and discussion

3.1. System response

The self-excited thermoacoustic oscillation was triggered under different mesh positions and mesh numbers to investigate the effect of varying mesh properties on the system oscillation frequency and amplitude. The system responses under different mesh positions and numbers are shown in Fig. 4. It can be seen that the both system eigenfrequency (f_{eigen}) and root mean squared amplitude (P_{rms}) present the similar trends across all cases as Φ increases. Specifically, f_{eigen} presents a decreasing trend with increasing Φ and becomes less varying with Φ when $\Phi > 1.8$ for most cases, while p_{rms} presents a trend of increase then decrease. The turning point of p_{rms} is located at $\Phi = 1.6$ for most cases. The trends of f_{eigen} and p_{rms} show that both mesh number and position have limited effects on the relationship between system response and Φ.

It has been reported that heat release and mean temperature play important roles in the system eigenfrequency [5]. Meanwhile, the Rayleigh Index suggests that the oscillation amplitude is related to the relative phase between the heat release and the pressure fluctuation [53]. Thus, the results suggest that the mesh has limited effects on influencing the changes in value and phase of heat release caused by the changes in Φ. By comparing the test results with and without a mesh (No Mesh), it can be seen that the f_{eigen} of No Mesh are lower than when a mesh was included, regardless of the mesh number and position. A difference of around 10 Hz in f_{eigen} can be found between the Mesh 30 and No Mesh cases, and approximately 5 Hz for the Mesh 10 and No Mesh. It can also be seen that the f_{eigen} decreases as the mesh number increases, and the maximum f_{eigen} under the same $\dot{m}_{CH_4}$ and Φ is obtained in Mesh 30, as shown in Fig. 4 (a). The f_{eigen} increases by approximately 6 Hz when changes the Mesh 10 to Mesh 30, and 4 Hz as the Mesh 10 changes to Mesh 20.

However, the f_{eigen} is not sensitive to the changes in mesh position compared to the cases with varied mesh numbers. From Fig. 4 (b), it can be seen that the f_{eigen} presents similar trends and values as the mesh moves from L/4 to L/12. Meanwhile, the difference in f_{eigen} is less than 1 Hz for most cases, while the f_{eigen} decreases by approximately 3 Hz when the mesh is placed at the upper end of the tube. Similarly, the f_{eigen} significantly decreases when the mesh is removed. These results show that the f_{eigen} is more significantly influenced by the mesh number than the mesh position.

It has been found that the addition of a mesh in the upstream region can lead to an increase of f_{eigen} [31], which is opposite to when the mesh is placed in the downstream region, as observed in this study. This opposite effect caused by the different mesh's placement position is possibly attributed to the higher mean acoustic speed in the tube due to the higher downstream mean temperature when the mesh is placed in the downstream region [26]. The presence of a mesh in the downstream region can diffuse the upward convective flow and heat flow to minimise

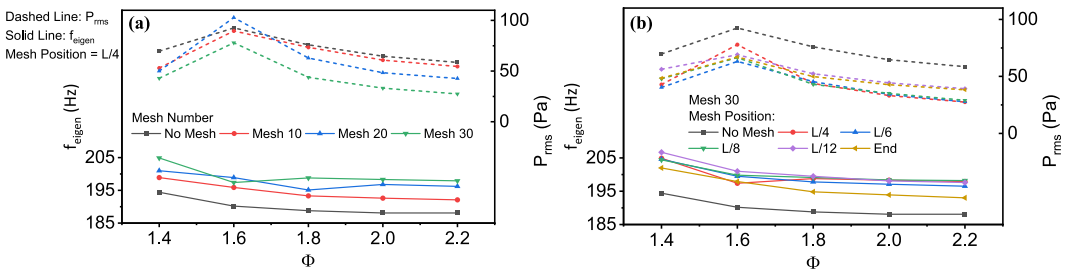

Fig. 4. Results of f_{eigen} and root mean square amplitude (p_{rms}) for the (a) different mesh number, (b) mesh position.

the temperature boundary layer, which results in a more uniform temperature profile after the mesh. At the same time, the heated mesh can also maintain the downstream temperature, resulting in a higher mean temperature and thus a greater mean acoustic speed in the tube. The temperature of the mesh will be further discussed in Section 3.2.

Similar findings can be obtained from the results of oscillation amplitude; the change in mesh number is more effectively influencing the f_{eigen} than the mesh position. From Fig. 4 (a), the oscillation amplitude is clearly suppressed when the mesh exists, as the p_{rms} of cases with a mesh is generally lower than No Mesh. The suppression effect of the mesh increases with an increasing mesh number. It can be seen that the values of p_{rms} for Mesh 30 are approximately half of those for the No Mesh, while Mesh 10 only slightly suppresses amplitude by approximately 5%. The ratio of p_{rms} for the cases with mesh (P_{rms}^{Mesh}) to the corresponding p_{rms} for No Mesh cases ($P_{rms}^{No\ Mesh}$) is obtained to represent the suppression effect of the mesh, as shown in Fig. 5. It can be seen that Mesh 10 has minimal effect on suppressing the oscillation, while Mesh 20 suppresses the oscillation amplitude by approximately 10% to 35%. Mesh 30 has the strongest suppression effect, as the oscillation amplitude decreases by about 20% to 55%. Therefore, a higher mesh number tends to have a greater suppression effect regardless of the mesh positions. However, it needs to be noted that the addition of a mesh can possibly trigger beating oscillation at $\Phi = 1.6$. Under such circumstances, the oscillation can potentially become more intense for the cases with mesh than No Mesh. Apart from $\Phi = 1.6$, the mesh presents good suppression effects on the oscillation. The suppression effect of mesh on the oscillation is likely caused by the changes in Rayleigh conductivity at the downstream region since the hole diameter is inversely related to the mesh number [32]. Meanwhile, the existence of a mesh in the downstream region could disturb and dampen the upward convective and heat flow due to the change in open area and the creation of vortices at the hole edges [35], leading to a damping effect for the system. The mesh can be therefore considered as an additional heat disturbance and fluctuation at the upper half of the tube. This can potentially result in the changes in Rayleigh index, indicating the less favourable phase between the fluctuations of heat release and pressure [54,55]. The temperature distribution of mesh and the flow conditions after the mesh will be discussed in the Section 3.2.

The RPs showing the effects of mesh on the recurrence of the system state are shown in Fig. 6. The diagonal structures, which consist of sets of gathered diagonal lines, can be observed from most of the cases in Fig. 6. The presence of diagonal structures indicates a periodic system with no noticeable state variation, negligible chaoticity, and relatively low complexity [23,52]. It can be seen that the diagonal structures are varied with the changing mesh numbers, as shown in Fig. 6 (a) to (d). For No Mesh cases, the diagonal structure presents sets of diagonal lines with clear continuity, and few scatter points can be observed near the diagonal structures. These clear diagonal structures and few scatter points imply the system with significant periodicities and less complexities. Similarly, RPs for Mesh 10, 20 and 30 are mainly formed by the diagonal lines, with the number of scatter points at the edges of each diagonal structure increasing as the mesh number rises, indicating the greater system complexity. For the Mesh 30 case, a curved pattern can be observed, as highlighted in Fig. 6 (d), whereas the Mesh 10 and 20 cases present straighter patterns of diagonal structure. The curved shape indicates interrupted diagonal lines at the curved position, which implies that there are slight changes in the system state under Mesh 30 at the L/4 position. Thus, the addition of mesh and the increase of mesh number can result in higher system complexity with more interruption in the system state.

Unlike the results of f_{eigen} and p_{rms} previously discussed, the change in mesh position can influence the system dynamics to a larger extent compared to the change in mesh number. For the Mesh 30 cases, the system generally exhibits periodic behaviour with few interruptions in system state when the mesh is positioned at L/4. However, as the mesh is moved to L/6, the system becomes quasi-periodic because beating oscillations are triggered. The RP for this case presents a different pattern from the other cases, as shown in Fig. 6 (e). The discontinuous diagonal structure represents noticeable changes in the system state whilst the bowed shape indicates similar evolution of states but with different velocities, which corresponds to different frequencies for the L/6 case [23]. At L/8, the system returns to a less complex system with periodic state, shown by the slightly curved diagonal structures consisting of diagonal lines in Fig. 6 (f). As the mesh keeps moving upwards to L/12,

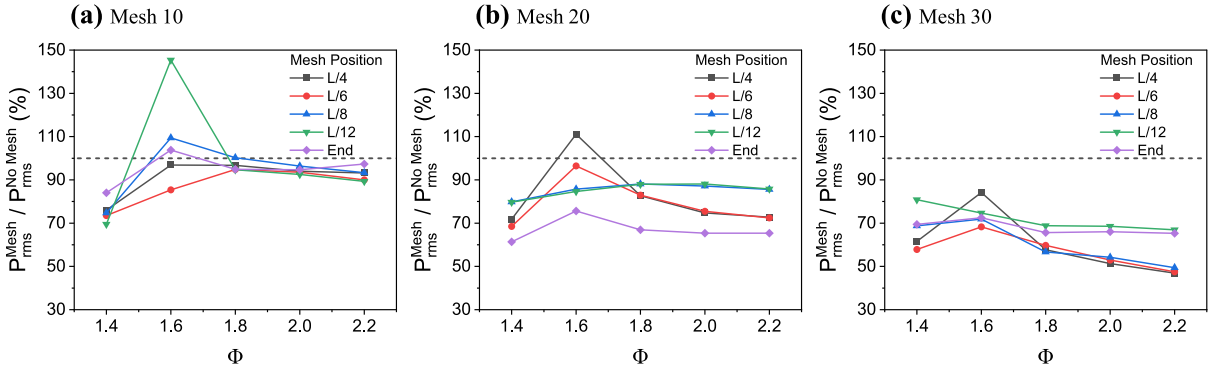

Fig. 5. Ratio of the cases with mesh to the corresponding cases without mesh under the same $\dot{m}_{CH_4}$. (a):Mesh 10; (b) Mesh 20; (c) Mesh 30.

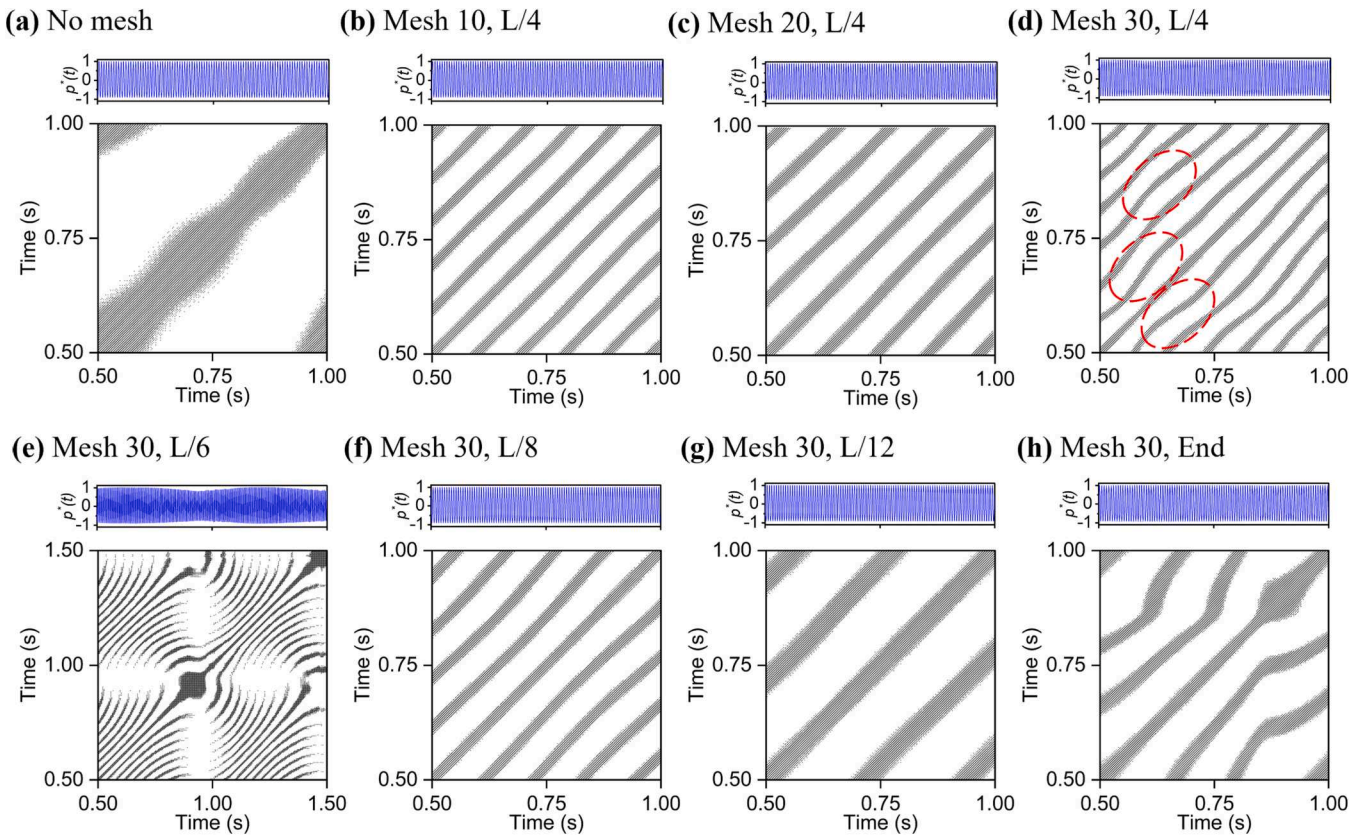

Fig. 6. The recurrence plot (RP) for the cases of L/4 at different mesh numbers of (a) No mesh, (b) Mesh 10, (c) Mesh 20 and (d) Mesh 30. And the case of Mesh 30 at different mesh positions of (e) L/6, (f) L/8, (g) L/12 and (h) top end. The embedding dimension is set to 3 for all RPs, and the τ is determined by the first zero-crossing point of the autocorrelation function.

as shown in Fig. 6 (g), the diagonal structures become straighter than L/8, indicating the system has more periodic natures and fewer system state changes [23,48]. When the mesh moves to the top end of tube, the system becomes less stable with noticeable system state changes, as shown by the clear curved shape in Fig. 6 (h).

Fig. 7 shows the RQA results for quantifying the system dynamics of the cases under different mesh numbers and two different mesh positions. It can be seen that the addition of mesh results in changes of DET, ADL and ENT, indicating that the mesh can influence the systems' dynamic properties. From Fig. 7 (a), the No Mesh case has the greatest DET and is generally stable when Φ changes, whereas the addition of a mesh decreases DET. It can also be found that the value of DET decreases as the mesh number increases, which represents a more complex system with less occurrence probability of similar system states at a higher mesh number. The result of ADL also presents an inverse relationship between mesh number and system parallelism, as shown in Fig. 7 (b). It indicates that the system state can be more frequently interrupted if the system includes a mesh, especially at a higher mesh number. The ENT for the cases with a mesh are generally greater than the cases without a mesh. The greater ENT for the cases with a mesh also indicates that the addition of a mesh could lead to a more random and complex system. It needs to be noted that the ENT for all cases is relatively small, which means the system generally present negligible chaoticity since no chaotic state is found, resulting in the small ENT values [6,23,26].

The mesh position can also influence the system dynamical properties, as shown in Fig. 8. It can be seen that the DET and ADL tend to deviate from No Mesh case as the mesh moves downwards, indicating the more effective role of the mesh in affecting system oscillation at a lower position. This may be caused by the enhanced convective flow due to the greater mean temperature of the mesh as the mesh is closer to the

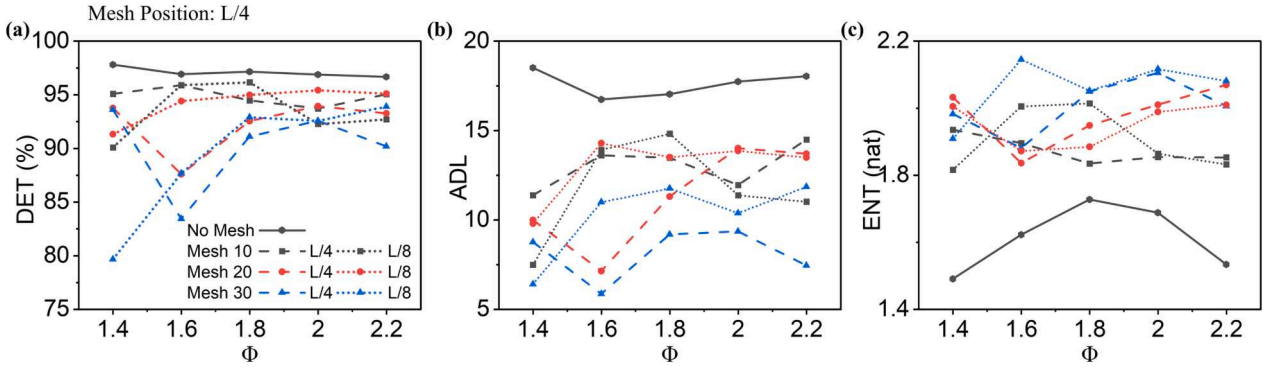

Fig. 7. RQA result for the cases with different mesh numbers.

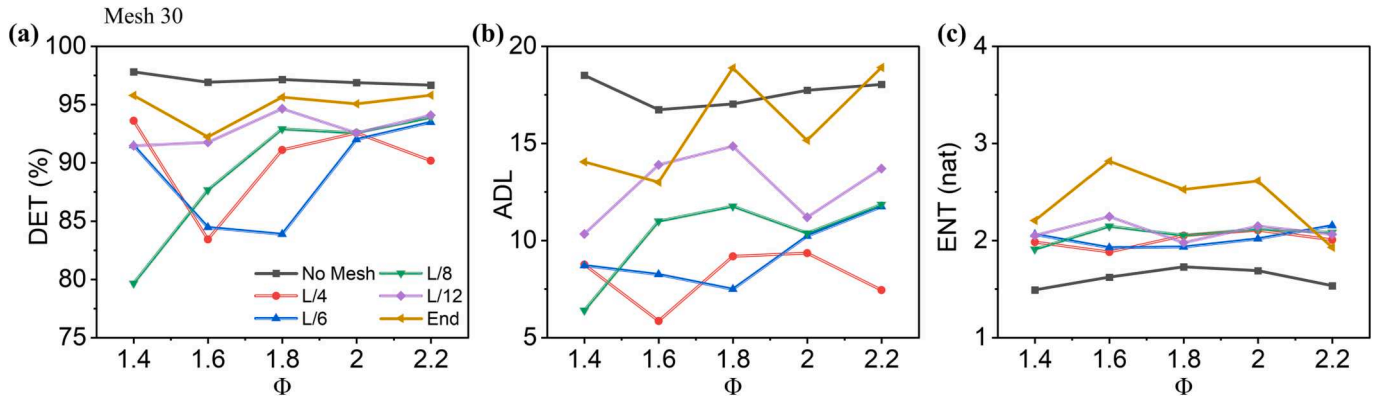

Fig. 8. RQA result for the comparison of different mesh positions.

flame, which means the stronger heating effect of radiation. The mean temperature of mesh will be discussed in section 3.2. However, the change in mesh position has limited effect on ENT, apart from the case where the mesh is at the top end. Therefore, it can be concluded that the mesh number and position can affect system dynamics to different extents, thus providing an additional means of altering the system disturbance and state.

3.2. Mechanism analysis

The results of system response in terms of f_{eigen}, p_{rms} and the system dynamics shows that the system can be significantly influenced by the mesh. As mentioned in the previous section, the mesh can act as an additional disturbance and fluctuation source of heat in the downstream region and can change the flow and heat conditions. Therefore, thermal imaging of the mesh and tube wall was conducted to discover the relationship between the mesh temperature and the system response. Meanwhile, schlieren images of the region post to the mesh were captured to indicate the change of flow and heat conditions caused by the mesh.

3.2.1. Mesh temperature analysis

In this study, a SWIR and LWIR camera were utilised to obtain the mesh and tube wall temperature, respectively. Example thermal images of different meshes are shown in Fig. 9. From the thermal images, it is found that the overall temperature of the mesh increases with the increasing mesh number, since Mesh 30 has the largest area where the temperature is above 300 °C, and the largest high-temperature area (above 515 °C). It is attributed to the enhanced heat transfer with the denser mesh (high mesh number). Its greater surface area and narrower spacing among the mesh wires result in enhanced heat transfer within the mesh. Besides, the mesh can block more convective hot flow, which increases the mesh temperature. The corresponding time evolution of (T^{mean}_{mesh}) for the cases in Fig. 9 are shown in Fig. 10. The obtained T^{mean}_{mesh} conforms to the observation of the hot area from the thermal images in Fig. 9. Mesh 30 has the highest temperature among them, with a

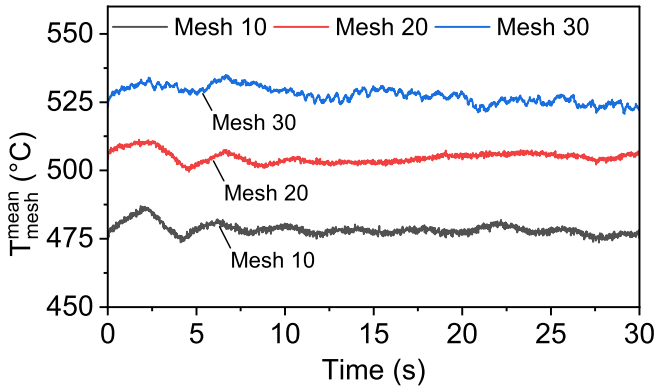

Fig. 10. Time evolution of T^{mean}_{mesh} for the cases conditions as $\dot{m}_{CH_4} = 0.8L/min$, $\Phi = 1.8$, at the mesh position of L/4.

temperature approximately 25 °C higher than Mesh 20, and 50 °C higher than Mesh 10. The temperature of Mesh 30 also presents more 'small' fluctuations in a smaller time-scale (e.g. from 10 to 20 s) than Mesh 20 and Mesh 10, indicating more intense heat transfer at the mesh. These results conform to the system dynamics analysis, where the Mesh 30 case tends to have a more complex system with more frequent variation of system state.

Similarly, the time evolution of T^{mean}_{mesh} at different positions for Mesh 30 are shown in Fig. 11. It can be found that the case of L/4 has the highest T^{mean}_{mesh} since the mesh is closer to the flame than the other positions, which means there is stronger direct heating of the mesh from the flame. As the mesh is moved upwards, the T^{mean}_{mesh} becomes less varied, until the mesh reaches the top end of the tube. Fig. 12 shows the time evolution of synchronised T^{mean}_{mesh} and the upper RMS envelope of the waveform for the pressure fluctuations (E^{upper}_{RMS}) for the case at L/4. The E^{upper}_{RMS} represents the fluctuations of the oscillation amplitude. From Fig. 12 (a), it can be seen that both T^{mean}_{mesh} and E^{upper}_{RMS} are relatively unstable

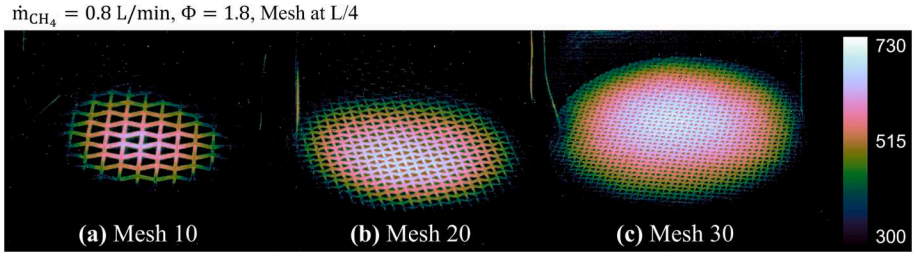

Fig. 9. Typical thermal images for the mesh with different mesh numbers under the condition of $\dot{m}_{CH_4} = 0.8L/min$, $\Phi = 1.8$, at the mesh position of L/4. Note that the size of the meshes are the same. The dark portion of the images represents the temperature that is lower than 300 °C.

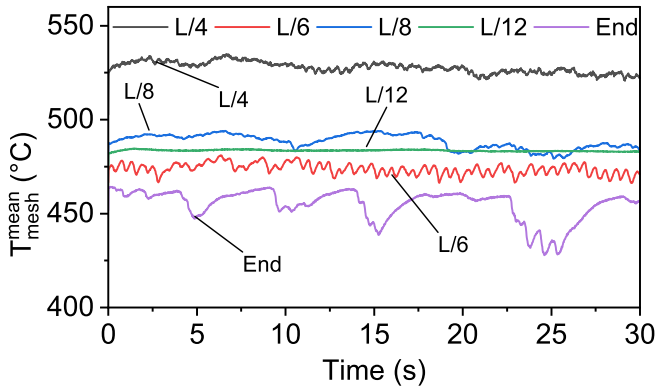

Fig. 11. Time evolution of T^{mean}_{mesh} for the cases of Mesh 30 at different mesh position, conditions as $\dot{m}_{CH_4} = 0.8L/min$, $\Phi = 1.8$.

and more time-variant. Although the changes in T^{mean}_{mesh} and E^{upper}_{RMS} are apparent, no periodic fluctuations for both T^{mean}_{mesh} and E^{upper}_{RMS} can be found from their time evolution. When the mesh is at L/6, the time evolution of the T^{mean}_{mesh} present the periodic fluctuations, and the temperature significantly decreases, as shown in Fig. 12 (b). It is caused by the intense amplitude fluctuations due to the beating oscillation triggered under this condition. It can be seen that the fluctuations of T^{mean}_{mesh} are in phase with the fluctuations of the oscillation amplitude, indicating the correlation between them. The presence of strong changes in the oscillation amplitude with time due to the beating oscillation can suppress the flame and result in the intense periodic disturbance of flow [2]. The intense disturbance may change the heat transfer at the mesh, resulting in periodic temperature fluctuations and the suppression of the flame, which in turn decreases the temperature.

As the mesh is moved to positions L/8 and L/12, the beating oscillation is no longer triggered. T^{mean}_{mesh} for L/8 still presents an apparent time-variant nature, however its lack of periodic nature is due to the absence of beating oscillation. The case of L/12 shows the stable time evolutions of T^{mean}_{mesh} and E^{upper}_{RMS} occurring at the same time, as shown in Fig. 12 (c). Once the mesh reaches the top end of the tube, the T^{mean}_{mesh} becomes unstable and significant changes again, as shown in Fig. 11. This may be caused by the more intense convection and complex flow conditions around the mesh. The mesh at the top end of the tube is in direct contact with low temperature ambient air, resulting in a large temperature gradient and enhanced convective flow. By comparing these cases under different conditions, it can be seen that the time evolution of T^{mean}_{mesh} and the fluctuations of oscillation amplitude (via E^{upper}_{RMS}) present similar characteristics and temporal synchronicity, indicating a strong correlation between mesh temperature and oscillation behaviour.

The time-averaged temperature ($\overline{T}_{mesh}$) for meshes with different mesh numbers and at different positions are shown in Fig. 13 (a) and Fig. 13 (b), respectively. It can be seen that the cases of Mesh 30 have generally greater $\overline{T}_{mesh}$ than the cases of Mesh 10 and 20 for both L/4 and L/8. The $\overline{T}_{mesh}$ of different mesh numbers conforms to the findings from the single frame thermal images shown in Fig. 9; that the higher mesh number tends to have a greater $\overline{T}_{mesh}$. Meanwhile, it can also be seen that the similar $\overline{T}_{mesh}$ is obtained at various Φ, unless a quasi-periodic oscillation is triggered (Φ = 1.6, Mesh 30, L/4). Fig. 13 (b) also validates that

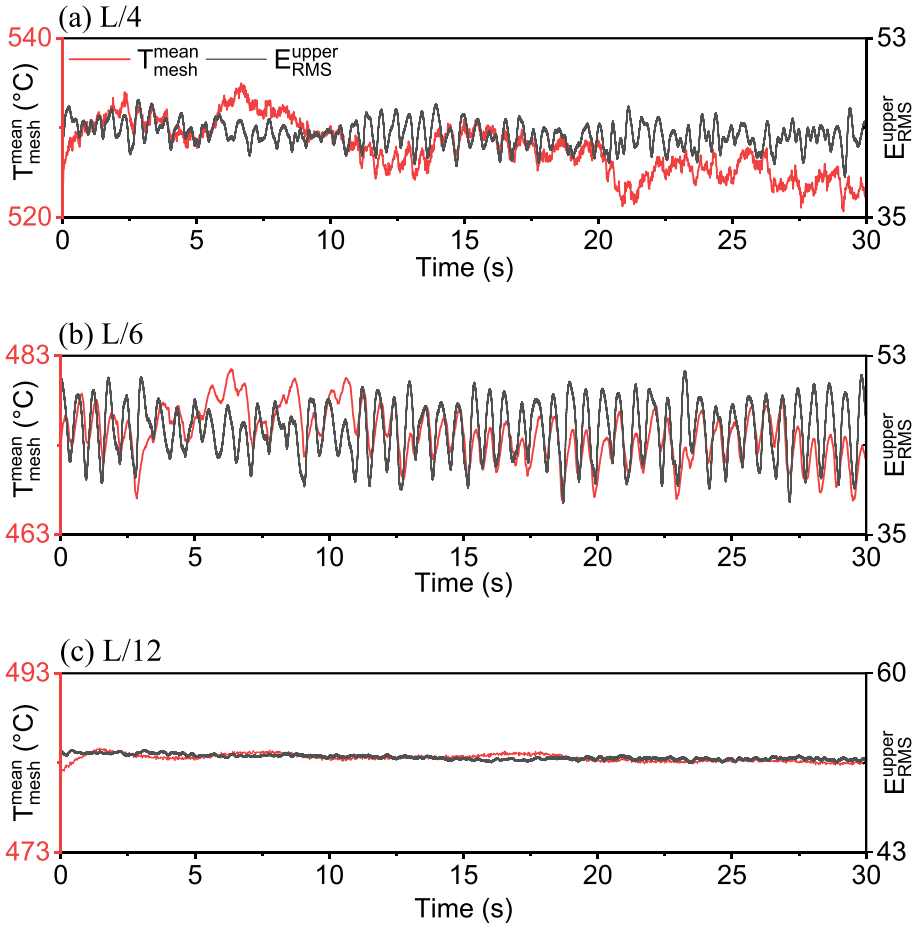

Fig. 12. Time evolution of synchronised T^{mean}_{mesh} and E^{upper}_{RMS} for the Mesh 30 cases under the condition of $\dot{m}_{CH_4} = 0.8L/min$, $\Phi = 1.8$, at different mesh position of (a) L/4, (b) L/6 and (c) L/12.

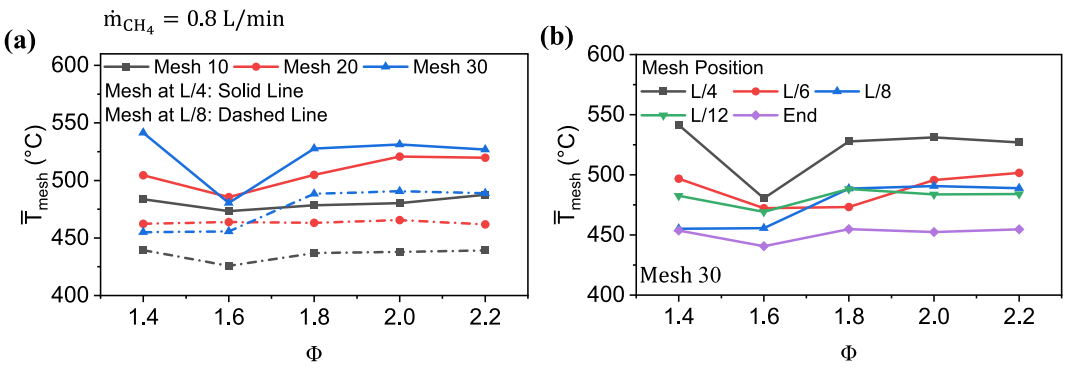

Fig. 13. $\overline{T}_{mesh}$ for the mesh under different: (a) Mesh number, and (b) Mesh position.

the $\overline{T}_{mesh}$ tends to decrease as the mesh is moved to a higher position, especially for the cases in the range where the system presents less time-varied properties ($\Phi > 1.8$) [25].

3.2.2. Schlieren imaging

The mesh at the downstream region can affect the upward convective flow and the heat conditions since the perforated structure of the mesh can effectively obstruct and diffuse the flow. The heated mesh can also act as an additional disturbance and fluctuation source of heat, influencing the heat transfer in the downstream region. Therefore, a schlieren system is utilised to visualise the heat flow in the region above the mesh. Note that schlieren images in this work only focused on two experimental conditions; No Mesh (1) and meshes with different mesh numbers located at the tube end (2).

The schlieren images for cases under different mesh numbers are shown in Fig. 14 (b)~(e). The existence of a mesh can result in different patterns of the schlieren, indicating changes in heat and flow conditions. The white dashed-dotted line at the top of Fig. 14 (b) highlights the region away from the tube end, where the hot flow is mainly driven by the convection outside the tube rather than the strong convection inside the tube. It can be seen that the flow pattern in the image of No Mesh is more complex than that of Mesh 30. Sharper edges of the pattern and stronger contrast can be observed from the image of No Mesh than Mesh 30, as shown in the region highlighted in Fig. 14 (b). This indicates a more complicated temperature distribution [43]. The time-averaged mean gradients in each image were calculated using the Prewitt method for the region of interest (highlighted by dashed-dotted line) to show the difference in the degree of inhomogeneities (via contrast level), shown in Fig. 14 (a). It can be seen that the time-averaged mean gradient in this region tends to decrease as the mesh number increases, indicating a smaller temperature gradient and more uniform temperature distribution in the highlighted region at a higher mesh number. These results indicate that a more complex flow pattern is obtained in No Mesh case, implying that the flow condition is less complex at higher mesh numbers. In addition, the difference in the time-averaged mean gradient between Mesh 10 and 20 is relatively small, while there is a clearer difference between Mesh 20 and Mesh 30. This shows that the heat and flow conditions might be nonlinearly related to the open area of the mesh.

The white dashed line in Fig. 14 highlights the region that is immediately after the mesh. A planar shape pattern can be found in the cases of Mesh 20 and Mesh 30, while the pattern is not apparent in the case of Mesh 10. For the case of No Mesh, no planar shape can be found. The sets of images to show the formation and the movement of the planar pattern are shown in Fig. 15. The start point of 0 ms is defined as when the hot flow starts to pass through the mesh. From 0 ms to 2 ms, the hot gas flow inside the tube is 'pumped' out through the mesh, as highlighted by the solid arrow. It can be seen at 1 ms that the hot flow is separated as the hot flow passes across the small hole of the mesh, forming several sub-flows. Meanwhile, the pattern of the sub-flow presents a profile that is determined by the boundary layer, indicating that the wire of the mesh can effectively influence the flow conditions by providing a shear force. As the hot flow passes through the mesh, the sub-flows begin to recombine, and the boundaries between sub-flows disappear after 2 ms. A planar pattern of the hot flow is then formed after the integrating process of the sub-flows, which is 3 ms after the hot flow passes the mesh, indicating that a uniform flow with a uniform temperature profile is formed. Once such flow with the planar temperature profile is generated, the stable flow keeps moving upward with a speed of approximately 1.25 m/s, and the planar temperature profile is sustained until the pattern disappears. After approximately 5 ms from the flow starts to pass through the mesh, a new flow starts forming, as

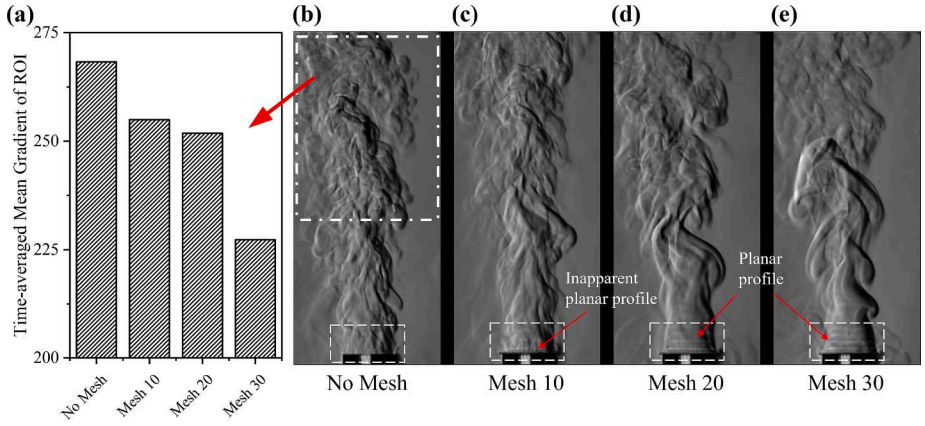

Fig. 14. (a) Time-averaged mean gradient of the region highlighted by dashed-dotted line. Schlieren images for the cases of b) No Mesh, (c) Mesh 10, (d) Mesh 20, (e) Mesh 30 under the condition of $\dot{m}_{CH_4} = 0.8L/min$, $\Phi = 1.8$.

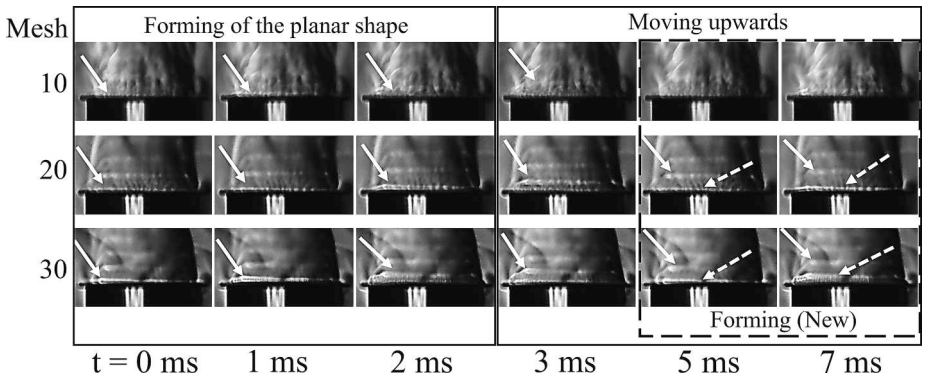

Fig. 15. Time evolution of the formation and movement of the planar shaped pattern for the cases of Mesh 10, 20 and 30.

highlighted by the dashed arrow. The presence of a planar pattern demonstrates the influence the mesh has on disturbing the flow and changing the heat transfer behaviour. In addition, the planar profile might be one of the reasons for less complex heat and flow conditions. The lower time-averaged mean gradients at the region highlighted by the dashed-dotted line in Fig. 14 (b) might also be caused by the planar profile.

3.2.3. Discussion

In summary, the results of thermal imaging show good agreement in the time domain between the time evolution of mesh temperature and the pressure oscillation. Meanwhile, the relatively high but fluctuated temperature can be obtained by the mesh regardless of changes in mesh number and position. These validate that the mesh can act as an additional disturbance and fluctuation source of heat in the downstream. Besides, comparing the RPs (as shown in Fig. 6) and the time evolution of T_{mesh}^{mean} (as shown in Fig. 10 and Fig. 11), it can be found that the degree of variation for the T_{mesh}^{mean} is in a good agreement with the results of RP. Compared to the cases of Mesh 10 and 20, the RP of Mesh 30 has curved shapes, which conforms to the more varied T_{mesh}^{mean} of Mesh 30 than Mesh 10 and 20. The cases with obvious pattern changes and curved shapes tend to have a greater variation of T_{mesh}^{mean} with time, such as the case of the mesh at L/6 and top end of the tube. In contrast, the case at L/12 has a slight variation of T_{mesh}^{mean}, of which the RP consists of straight diagonal structures with few interrupted diagonal lines and scatter points. The agreements between the time evolution of T_{mesh}^{mean} and the results of RP evidence the correlation between the mesh temperature and system dynamics.

The results of schlieren imaging further evidence that the mesh can influence both the heat and flow conditions, since the diffusion of flow and the formation of planar pattern can be obtained when the mesh is placed. The results also show that the greater effectiveness of mesh on affecting the heat and flow conditions is obtained by a higher mesh number.

Based on the results of the thermal and schlieren imaging, it can be summarised that the effects of a mesh on the system response are mainly caused by the changes of heat and flow conditions in the downstream region. It has been found that the downstream flow is critical to the oscillation frequency and amplitude, and the disturbance to the downstream flow can suppress oscillation to varied extents [38]. In this study, the buoyancy effect of the convective flow can be strong due to the greater temperature at a higher mesh number. This leads to more unsteady heat release of the mesh, which can be evidenced by the more frequently fluctuating temperature of Mesh 30, as shown in Fig. 10. Meanwhile, the smaller open area of Mesh 30 can diffuse and obstruct the flow more effectively, shown by the schlieren images in Fig. 14. The disturbance of the convective flow, and the additional unsteady heat disturbance and fluctuation source (heated mesh) can lead to an unfavourable phase difference between the heat and pressure fluctuations, resulting in the suppression of the self-excited thermoacoustic oscillation. The mean temperature in the downstream region can become higher at a higher mesh number due to the obstruction of the upwards convective flow and greater temperature of the mesh, as shown in Fig. 16 (a). The increase in mean temperature leads to the increase of mean acoustic speed in the tube, which results in a higher f_{eigen} of oscillation [26].

Although the change in mesh position also causes the change in $\overline{T}_{mesh}$, the f_{eigen} and p_{rms} values are not sensitive to the mesh position. Instead, it indicates that the open area is critical to the system response. As the mesh is moved upwards, the region that is affected by the disturbance and heating effect from the mesh decreases, as shown in Fig. 16 (b). The fewer changes in mean acoustic speed inside the tube and fewer effects of disturbance are possibly resulted into, leading to the less obvious changes in f_{eigen} and p_{rms}. Also, the mesh can act as an acoustic reflection boundary because the size of the mesh hole is smaller than the wavelength of the self-excited oscillation, and the velocity potential can change when the pressure wave passes through the hole [56,57]. Thus, the changes in mesh position cause the changes in acoustic properties of the resonance chamber (tube) since the acoustic reflection boundary changes. The low sensitivity of f_{eigen} and p_{rms} to mesh position changes implies that the changes in acoustic boundaries have only limited influences in changing the system response.

4. Conclusions

In this study, the effects on the self-excited thermoacoustic oscillation of adding a mesh into the downstream region of a Rijke tube were investigated. The system response and dynamic properties were obtained based on the measured pressure fluctuations time series. The recurrence analysis, including the recurrence plot (RP) and recurrence quantification analysis (RQA), was conducted to investigate the system dynamics qualitatively and quantitively. A thermal imaging system consisting of a long wavelength infrared (LWIR) camera and a short wavelength infrared (SWIR) camera was utilised to obtain the temperature distributions of the mesh and tube wall. The time-evolution of mesh mean temperature (T_{mesh}^{mean}) and the time-averaged T_{mesh}^{mean} ($\overline{T}_{mesh}$) were obtained from the time sequence images captured by the SWIR camera. A high-speed Schlieren imaging system was also employed to visualise inhomogeneities above the mesh, thereby revealing the effect of mesh on the heat and flow conditions. The conclusions that can be drawn from this study are:

- The addition of a mesh can affect the system response in terms of the oscillation frequency and amplitude, and the system dynamical properties. Changing the mesh number and/or position can lead to changes in the mesh effectiveness on influencing the system.
- The suppression effect of the mesh on the oscillation amplitude was discovered. The oscillation was more suppressed at a high mesh

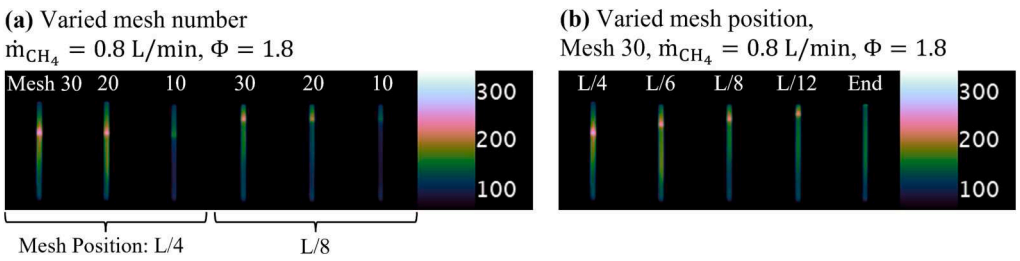

Fig. 16. Tube wall temperature measured by LWIR camera for the cases conditions as $\dot{m}_{CH_4} = 0.8L/min$, $\Phi = 1.8$ for comparison of (a) Varied mesh number, (b) Varied mesh position. The tube wall temperature is measured after the stabilisation process, which means the temperature is stable and can be used to approximately indicate the temperature profile inside the tube.

number, by up to 50 % in terms of the root mean square amplitude. Meanwhile, the frequency increases with the increasing mesh number. The oscillation frequency and amplitude were insensitive to mesh position changes.

- A more complex system with more interruptions of the system state can be resulted when the mesh is included. The system dynamic properties can be sensitive to both the changes in mesh number and position. Quasi-periodic oscillations could be triggered at specific mesh numbers and positions.
- The change in mesh number was found to have limited effects on the variation of T^{mean}_{mesh} in time domain but significantly affect the $\overline{T}_{mesh}$ varying with Φ. However, the degree of T^{mean}_{mesh} variation in time domain and $\overline{T}_{mesh}$ varying with Φ were sensitive to changes in the mesh position. The agreements between the variation of T^{mean}_{mesh} and system dynamics were obtained.
- The schlieren images proved the effects of a mesh on influencing the heat and flow conditions above the mesh. A more complex pattern with greater contrast was obtained at a lower mesh number and when tested without a mesh. The formation of the planar shape pattern immediately after the mesh indicated the planar temperature profile caused by the mesh.

CRediT authorship contribution statement

Xuanqi Liu: Conceptualization, Methodology, Software, Formal analysis, Investigation, Writing – original draft, Writing – review & editing, Visualization. **Yufeng Lai:** Validation, Writing – original draft, Writing – review & editing, Formal analysis, Investigation, Resources. **Callum Fisk:** Writing – review & editing, Methodology, Software. **Jon Willmott:** Writing – review & editing, Methodology, Software. **Huaichun Zhou:** Writing – review & editing. **Yang Zhang:** Supervision, Resources.

Declaration of Competing Interest

The authors declare that they have no known competing financial interests or personal relationships that could have appeared to influence the work reported in this paper.

Data availability

Data will be made available on request.

Acknowledgement

The authors wish to acknowledge Transforming Foundation Industries Network+ (EPSRC grant EP/V026402/1) for partly funding this work.

References

[1] H. Gotoda, H. Nikimoto, T. Miyano, S. Tachibana, Dynamic properties of combustion instability in a lean premixed gas-turbine combustor, Chaos. 21 (2011), https://doi.org/10.1063/1.3563577.
[2] F. Weng, S. Li, D. Zhong, M. Zhu, Investigation of self-sustained beating oscillations in a Rijke burner, Combust. Flame. 166 (2016) 181–191, https://doi.org/10.1016/j.combustflame.2016.01.016.
[3] D. Zhao, Y. Guan, A. Reinecke, Characterizing hydrogen-fuelled pulsating combustion on thermodynamic properties of a combustor, Commun. Phys. 2 (2019), https://doi.org/10.1038/s42005-019-0142-8.
[4] D. Zhao, Z.H. Chow, Thermoacoustic instability of a laminar premixed flame in Rijke tube with a hydrodynamic region, J. Sound. Vib. 332 (2013) 3419–3437, https://doi.org/10.1016/j.jsv.2013.01.031.
[5] H. Zhao, G. Li, D. Zhao, Z. Zhang, D. Sun, W. Yang, S. Li, Z. Lu, Y. Zheng, Experimental study of equivalence ratio and fuel flow rate effects on nonlinear thermoacoustic instability in a swirl combustor, Appl. Energy. 208 (2017) 123–131, https://doi.org/10.1016/j.apenergy.2017.10.061.
[6] R.I. Sujith, S.A. Pawar, Thermoacoustic Instability, Springer International Publishing, Cham, 2021. Doi: 10.1007/978-3-030-81135-8.
[7] Rayleigh,, The explanation of certain acoustical phenomena 1, Nature. 18 (1878) 319–321, https://doi.org/10.1038/018319a0.
[8] G. Wu, X. Jin, Q. Li, H. Zhao, I.R. Ahmed, J. Fu, Experimental and numerical definition of the extreme heater locations in a closed-open standing wave thermoacoustic system, Appl. Energy. 182 (2016) 320–330, https://doi.org/10.1016/j.apenergy.2016.08.104.
[9] H. Zhou, Z. Liu, C. Tao, M. Zhou, Mitigating self-excited thermoacoustic oscillations in a liquid fuel combustor using dual perforated plates, J. Acoust. Soc. Am. 148 (2020) 1756–1766, https://doi.org/10.1121/10.0002007.
[10] S. Candel, Combustion dynamics and control: Progress and challenges, Proceedings of the Combustion Institute. 29 (2002) 1–28. Doi: 10.1016/S1540-7489(02)80007-4.
[11] X. Li, Y. Huang, D. Zhao, W. Yang, X. Yang, H. Wen, Stability study of a nonlinear thermoacoustic combustor: Effects of time delay, acoustic loss and combustion-flow interaction index, Appl. Energy. 199 (2017) 217–224, https://doi.org/10.1016/j.apenergy.2017.04.074.
[12] M.P. Juniper, R.I. Sujith, Sensitivity and nonlinearity of thermoacoustic oscillations, Ann. Rev. Fluid. Mech. 50 (2018) 661–689, https://doi.org/10.1146/annurev-fluid-122316.
[13] V. Godavarthi, P. Kasthuri, S. Mondal, R.I. Sujith, N. Marwan, J. Kurths, Synchronization transition from chaos to limit cycle oscillations when a locally coupled chaotic oscillator grid is coupled globally to another chaotic oscillator, Chaos. 30 (2020), https://doi.org/10.1063/1.5134821.
[14] K. Balasubramanian, R.I. Sujith, Thermoacoustic instability in a Rijke tube: Non-normality and nonlinearity, Phys. Fluids. 20 (2008), 044103, https://doi.org/10.1063/1.2895634.
[15] N. Swaminathan, G. Xu, A.P. Dowling, R. Balachandran, Heat release rate correlation and combustion noise in premixed flames, J. Fluid. Mech. 681 (2011) 80–115, https://doi.org/10.1017/jfm.2011.232.
[16] D. Ebi, A. Denisov, G. Bonciolini, E. Boujo, N. Noiray, Flame Dynamics Intermittency in the Bistable Region Near a Subcritical Hopf Bifurcation, J. Eng. Gas. Turbine. Power. 140 (2018), https://doi.org/10.1115/1.4038326.
[17] Y. Sun, Z. Rao, D. Zhao, B. Wang, D. Sun, X. Sun, Characterizing nonlinear dynamic features of self-sustained thermoacoustic oscillations in a premixed swirling combustor, Appl. Energy. 264 (2020), https://doi.org/10.1016/j.apenergy.2020.114698.
[18] V. Nair, G. Thampi, R.I. Sujith, Intermittency route to thermoacoustic instability in turbulent combustors, J. Fluid. Mech. 756 (2014) 470–487, https://doi.org/10.1017/jfm.2014.468.
[19] K. Kashinath, I.C. Waugh, M.P. Juniper, Nonlinear self-excited thermoacoustic oscillations of a ducted premixed flame: Bifurcations and routes to chaos, J. Fluid. Mech. 761 (2014) 399–430, https://doi.org/10.1017/jfm.2014.601.
[20] H. Kobayashi, H. Gotoda, S. Tachibana, S. Yoshida, Detection of frequency-mode-shift during thermoacoustic combustion oscillations in a staged aircraft engine model combustor, J. Appl. Phys. 122 (2017), https://doi.org/10.1063/1.5003912.
[21] L. Ji, J. Wang, W. Zhang, D. Li, G. Hu, Z. Huang, Nonlinear dynamic characteristics of self-excited thermoacoustic instabilities in premixed swirling flames, Exp.

Therm. Fluid. Sci. 150 (2024), 111033, https://doi.org/10.1016/j.expthermflusci.2023.111033.
[22] V. Nair, R.I. Sujith, Intermittency as a transition state in combustor dynamics: an explanation for flame dynamics near lean blowout, Combust. Sci. Technol. 187 (2015) 1821–1835, https://doi.org/10.1080/00102202.2015.1066339.
[23] N. Marwan, M. Carmenromano, M. Thiel, J. Kurths, Recurrence plots for the analysis of complex systems, Phys. Rep. 438 (2007) 237–329, https://doi.org/10.1016/j.physrep.2006.11.001.
[24] J. O'Connor, Understanding the role of flow dynamics in thermoacoustic combustion instability, Proceedings of the Combustion Institute. (2022). Doi: 10.1016/j.proci.2022.07.115.
[25] X. Liu, H. Zhou, Y. Lai, Y. Zhang, Equivalence ratio independence and dependence ranges of system responses for a nonlinear thermoacoustic oscillation in a Rijke tube, J. Sound. Vib. (2022), 117545, https://doi.org/10.1016/j.jsv.2022.117545.
[26] X. Liu, H. Zhou, Y. Lai, Y. Zhang, Characterisations of self-excited nonlinear oscillations at varied system parameters in a Rijke tube with a premixed laminar flame, Exp. Therm. Fluid. Sci. 146 (2023), 110923, https://doi.org/10.1016/j.expthermflusci.2023.110923.
[27] X. Yu, K. Ma, X. Li, D. Zhao, B. Shi, Forced swirl tubular flame under different equivalence ratios and oxygen mole fractions, Exp. Therm. Fluid. Sci. 147 (2023), 110948, https://doi.org/10.1016/j.expthermflusci.2023.110948.
[28] J. Kim, M. Jang, K. Lee, A.R. Masri, Experimental study of the beating behavior of thermoacoustic self-excited instabilities in dual swirl combustors, Exp. Therm. Fluid. Sci. 105 (2019) 1–10, https://doi.org/10.1016/j.expthermflusci.2019.03.007.
[29] X. Li, D. Zhao, X. Yang, H. Wen, X. Jin, S. Li, H. Zhao, C. Xie, H. Liu, Transient growth of acoustical energy associated with mitigating thermoacoustic oscillations, Appl. Energy. 169 (2016) 481–490, https://doi.org/10.1016/j.apenergy.2016.01.060.
[30] P. Pancharia, V. Ramanan, R. Sampath, S.R. Chakravarthy, Effect of inlet flow turbulence on flame–vortex dynamics during thermo-acoustically induced flame flashback in a premixed dump combustor, Exp. Therm. Fluid. Sci. 139 (2022), 110733, https://doi.org/10.1016/j.expthermflusci.2022.110733.
[31] H. Zhou, Z. Liu, H. Fang, C. Tao, M. Zhou, L. Hu, Attenuation effects of perforated plates with heterogeneously distributed holes on combustion instability in a spray flame combustor, J. Mech. Sci. Technol. 34 (2020) 4865–4875, https://doi.org/10.1007/s12206-020-1042-2.
[32] N. Tran, S. Ducruix, T. Schuller, Passive control of the inlet acoustic boundary of a swirled burner at high amplitude combustion instabilities, J. Eng. Gas. Turbine. Power. 131 (2009), https://doi.org/10.1115/1.3078206.
[33] N. Tran, S. Ducruix, T. Schuller, Damping combustion instabilities with perforates at the premixer inlet of a swirled burner, Proceedings of the Combustion Institute. 32 II (2009) 2917–2924. Doi: 10.1016/j.proci.2008.06.123.
[34] C. Lawn, The acoustic impedance of perforated plates under various flow conditions relating to combustion chamber liners, Appl. Acoustics. 106 (2016) 144–154, https://doi.org/10.1016/j.apacoust.2016.01.005.
[35] M.A. Temiz, J. Tournadre, I.L. Arteaga, A. Hirschberg, Non-linear acoustic transfer impedance of micro-perforated plates with circular orifices, J. Sound. Vib. 366 (2016) 418–428, https://doi.org/10.1016/j.jsv.2015.12.022.
[36] T. Luong, M.S. Howe, R.S. McGowan, On the Rayleigh conductivity of a bias-flow aperture, J. Fluids. Struct. 21 (2005) 769–778, https://doi.org/10.1016/j.jfluidstructs.2005.09.010.
[37] L. Xu, G. Zhang, G. Wang, Z. Feng, X. Tian, L. Li, F. Qi, Effects of acoustic liner on thermoacoustic instabilities in a premixed swirl combustor, Aerosp. Sci. Technol. 118 (2021), https://doi.org/10.1016/j.ast.2021.107070.
[38] D. Zhao, E. Gutmark, A. Reinecke, Mitigating self-excited flame pulsating and thermoacoustic oscillations using perforated liners, Sci. Bull. (Beijing). 64 (2019) 941–952, https://doi.org/10.1016/j.scib.2019.05.004.
[39] G. Zhang, X. Wang, L. Li, X. Sun, Effects of perforated liners on controlling combustion instabilities in annular combustors, AIAA. J. 58 (2020) 3100–3114, https://doi.org/10.2514/1.J059099.
[40] X. Jing, X. Sun, Experimental investigations of perforated liners with bias flow, J. Acoust. Soc. Am. 106 (1999) 2436–2441, https://doi.org/10.1121/1.428128.
[41] C. Lawn, Acoustic pressure losses in woven screen regenerators, Applied. Acoustics. 77 (2014) 42–48, https://doi.org/10.1016/j.apacoust.2013.09.019.
[42] A.P. Dowling, The calculation of thermoacoustic oscillations, J. Sound. Vib. 180 (1995) 557–581, https://doi.org/10.1006/JSVI.1995.0100.
[43] Y. Lai, A. Albadi, X. Liu, M. Davies, M. Hobbs, J. Willmott, Y. Zhang, Investigation of forced flow orientations on the burning behaviours of wooden rods using a synchronised multi-imaging system, Proc. Combust. Institute. (2022), https://doi.org/10.1016/j.proci.2022.07.057.
[44] Y. Lai, X. Wang, T.B.O. Rockett, J.R. Willmott, Y. Zhang, Investigation into wind effects on fire spread on inclined wooden rods by multi-spectrum and schlieren imaging, Fire. Saf. J. 127 (2022), https://doi.org/10.1016/j.firesaf.2021.103513.
[45] C. Zhu, M.J. Hobbs, J.R. Willmott, An accurate instrument for emissivity measurements by direct and indirect methods, Meas. Sci. Technol. 31 (2020), https://doi.org/10.1088/1361-6501/ab5e9b.
[46] American Society of Heating Refrigerating and Air-Conditioning Engineers, ASHRAE Handbook - Fundamentals, SI Edition, American Society of Heating, Refrigerating and Air-Conditioning Engineers, Atlanta, 2009.
[47] H. Gotoda, Y. Shinoda, M. Kobayashi, Y. Okuno, S. Tachibana, Detection and control of combustion instability based on the concept of dynamical system theory, Phys. Rev. E. Stat. Nonlin. Soft. Matter. Phys. 89 (2014), https://doi.org/10.1103/PhysRevE.89.022910.
[48] M. Murugesan, S. Balusamy, S. Hochgreb, L.K.B. Li, Recurrence analysis of forced synchroniza-tion in a self-excited thermoacoustic system, 24th International Congress on Sound and Vibration, ICSV 2017. (2017). Doi: Doi: 10.17863/CAM.33084.
[49] F. Takens, Detecting strange attractors in turbulence, in: 1981: pp. 366–381. Doi: 10.1007/BFb0091924.
[50] S. Schinkel, O. Dimigen, N. Marwan, Selection of recurrence threshold for signal detection, Eur. Phys. J. Spec. Top. 164 (2008) 45–53, https://doi.org/10.1140/epjst/e2008-00833-5.
[51] H. Zan, W. Zhou, X. Xiao, L. Lin, J. Zhang, H. Li, Recurrence network analysis for uncovering dynamic transition of thermo-acoustic instability of supercritical hydrocarbon fuel flow, Aerosp. Sci. Technol. 85 (2019) 1–12, https://doi.org/10.1016/j.ast.2018.11.040.
[52] N. Marwan, How to avoid potential pitfalls in recurrence plot based data analysis, Int. J. Bifurcation. Chaos. 21 (2011) 1003–1017, https://doi.org/10.1142/S0218127411029008.
[53] L. Magri, M.P. Juniper, J.P. Moeck, Sensitivity of the Rayleigh criterion in thermoacoustics, J. Fluid. Mech. 882 (2020) R1, https://doi.org/10.1017/jfm.2019.860.
[54] R.L. Raun, M.W. Beckstead, J.C. Finlinson, K.P. Brooks, A review of Rijke tubes, Rijke burners and related devices, Prog. Energy. Combust. Sci. 19 (1993) 313–364, https://doi.org/10.1016/0360-1285(93)90007-2.
[55] B. Entezam, W.K. Van Moorhem, J. Majdalani, Two-dimensional numerical verification of the unsteady thermoacoustic field inside a Rijke-type pulse combustor, Numeri. Heat. Transf. A. Appl. 41 (2002) 245–262, https://doi.org/10.1080/10407780252780153.
[56] J.W. Strutt, The Theory of Sound, Cambridge University Press (2011), https://doi.org/10.1017/CBO9781139058094.
[57] Rayleigh, XXXVII. On the passage of waves through apertures in Plane screens, and allied problems, The London, Edinburgh, and Dublin Philosoph. Magazine J. Sci. 43 (1897) 259–272. Doi: 10.1080/14786449708620990.